ULTRASOUND SIMULATIONS USING COMPUTED TOMOGRAPHY IMAGES AS PRIORS

by

Mert Tuzer

B.S., Physics, Boğaziçi University, 2012

Submitted to the Institute for Graduate Studies in
Science and Engineering in partial fulfillment of
the requirements for the degree of
Master of Science

Graduate Program in Physics
Boğaziçi University

2015

ULTRASOUND SIMULATIONS USING COMPUTED TOMOGRAPHY IMAGES AS PRIORS

APPROVED BY:

Assoc. Prof. Mehmet Burçin Ünlü (Thesis Supervisor)	.....
Assoc. Prof. Burak Acar (Thesis Co-supervisor)	.....
Assoc. Prof. Özhan Özatay	.....
Assist. Prof. Evren Özarslan	.....
Assist. Prof. Deniz Sezer	.....

DATE OF APPROVAL: 31.07.2015

ACKNOWLEDGEMENTS

In the first place, I would like to thank my thesis supervisors Assoc. Prof. Mehmet Burçin Ünlü and Assoc. Prof. Burak Acar for all the time and effort they spend during the preparation of my thesis.

I would like to thank my friends from the groups VAVlab and Medical and Biological Physics Research Group for expressing their valuable opinions about my work.

I would like to thank all my friends who know who they are for being there and supporting me.

Last but not least, I would like to thank my family for their patience and support during the preparation of my thesis.

This thesis has been supported by TUBITAK-TEYDEB 1505 Program, Grant # 5130002.

ABSTRACT

ULTRASOUND SIMULATIONS USING COMPUTED TOMOGRAPHY IMAGES AS PRIORS

Medical ultrasound system is one of the most ubiquitous imaging modalities in the world. In addition to the noninvasive nature of it, being low-cost and portable compared to other modalities makes it wide-spread in hospitals. Such common usage of the system needs more ultrasound technicians, or sonographers, and consequently training of new ones which requires at least a patient and an expert and almost a year to be a sonographer at last. In this phase, ultrasound simulators act a key role which reduces the need of human and cost factor significantly. The need for such real-time simulators has caused various works suggested in this area. They basically either interpolates pre-recorded ultrasound images (interpolative methods) or generates ultrasound images using other modalities i.e, computed tomography, magnetic resonance imaging (generative methods). The drawbacks of these methods respectively are incapability of simulating with various probe positions (view-dependent) and lacking realism due to not solving the wave physics exactly. In this thesis, a real-time ray-based generative ultrasound simulator using the computed tomography images will be presented. The novalties in this work are emanating multi-rays from each transducer element instead of single ray transmission by each of the element and two speckle models based on a local entropy map of computer tomography images and a machine learning algorithm in which some pairs of computer tomography images and ultrasound images of the same body slice are used.

ÖZET

BİLGİSAYARLI TOMOGRAFİ'YE DAYALI ULTRASON GÖRÜNTÜLEME SİMULASYONLARI

Medikal ultrason sistemleri dünyada en yaygın kullanılan sistemlerden biridir. Zararsız olmasının yanında, düşük maliyetli ve portatif olması, ultrasonun diğer sistemlere göre daha yaygın olarak kullanılmasını sağlamaktadır. Bu kadar yaygın kullanılması, daha fazla ultrason teknisyenlerinin eğitimini gerektirmektedir ki bu eğitim de en az bir hasta (gönüllü), bir uzman ve epey süre istemektedir. İşte burada devreye ultrason simulatörleri girmektedir. Gerçek zamanlı, bu denli simulasyonlara ihtiyaçtan dolayı bu alanda bir çok çalışma yapılmıştır. Genel olarak, ya önceden kaydedilmiş ultrason görüntüleri aradeğerlendirilmektedir, ya da bilgisayarlı tomografi, manyetik rezonans görüntüleme imgeleri üzerinden ultrason görüntüleri üretilmektedir. İlk kategorideki simulatörlerin dezavantajı farklı prob pozisiyonlarında simulasyonun doğru çalışamaması iken, ikinci kategorideki simulatörler, fiziksel mekanizmaları tam olarak çözmediği için gerçeklikten yoksundur. Bu tezde, bilgisayarlı tomografi imgelerine dayalı, gerçek zamanlı çalışan, ışın bazlı ultrason simulatörü sunulacaktır. Bu çalışmadaki yenilikler, her bir prob elemanından bir ışın yerine çoklu ışın göndermek ve biri bilgisayarlı tomografi imgelerinin yerel entropisine dayalı; diğeri aynı vücut bölgesinin bilgisayarlı tomografi ve ultrason imge ikililerini kullanan bir makine öğrenim algoritmasına dayalı benek gürültüsü (speckle noise) modelleridir.

TABLE OF CONTENTS

ACKNOWLEDGEMENTS . . . iii
ABSTRACT . . . iv
ÖZET . . . v
LIST OF FIGURES . . . viii
LIST OF TABLES . . . xii
LIST OF SYMBOLS . . . xiii
LIST OF ACRONYMS/ABBREVIATIONS . . . xiv
1. INTRODUCTION . . . 1
2. ULTRASOUND BACKGROUND: PHYSICS, IMAGING, SIMULATIONS . . . 5
2.1. Ultrasound Physics . . . 5
2.1.1. Sound Waves . . . 5
2.1.2. Wave In Media . . . 6
2.2. Ultrasound Imaging . . . 8
2.2.1. Transducers . . . 10
2.2.2. Imaging Modes . . . 10
2.2.3. Beamforming and Postprocessing . . . 12
2.2.4. Image Specifications . . . 14
2.3. Ultrasound Simulations . . . 16
2.3.1. Interpolative Methods . . . 17
2.3.2. Generative Methods . . . 18
3. CT BASED ULTRASOUND SIMULATION . . . 25
3.1. Single Ray Method . . . 26
3.1.1. Domain Modeling . . . 26
3.1.2. Ray Sampling . . . 26
3.1.3. Ray Simulation . . . 28
3.2. Speckle Modeling . . . 30
3.2.1. Local Entropy Based Model . . . 32
3.2.2. A Supervised Learning Approach . . . 34
3.3. Single Ray Beam Formation . . . 36

3.4. Multi Ray Beam Formation 38
4. RESULTS 40
5. DISCUSSION AND CONCLUSION 44
REFERENCES 46

LIST OF FIGURES

Figure 1.1. The figure (a) is the US image of the liver acquired with the curved transducer Toshiba Aplio 500. The figure (b) is the transducer employed in the process [1]. 1

Figure 1.2. The figure (a) shows a CT machine [2] and the figure (b) is an abdominal CT image. 3

Figure 1.3. Estimated imaging exams taken in the U.S. and the World in the year 2000 [3]. 3

Figure 2.1. Wave encountering with a different medium larger than its wavelength. 7

Figure 2.2. The figure left is the image of the liver obtained with a transducer at 4 MHz while on the right one is the image of the same liver portion acquired with a transducer operating at 6 MHz [4]. . . . 8

Figure 2.3. The process of acquiring A-mode signal [5]. 9

Figure 2.4. Types of transducers [6]. 10

Figure 2.5. B-mode (upper right) image and M-mode signal (below) of the mitral valve [3]. 11

Figure 2.6. The image left is color coded Doppler US on top of B-mode image which stays on right side [7]. 12

Figure 2.7. The mechanism of beamforming based on calculation of delays τ of each element [8]. 13

Figure 2.8. The firing mechanism of phased array transducers [5]. 13

Figure 2.9. The scan conversion of scan lines [9]. 14

Figure 2.10. Some of the artifacts [10]. 16

Figure 2.11. Some of the characteristics in usual US images. 16

Figure 2.12. The UltraSim simulator system and the user interface of the simulator [11]. 19

Figure 2.13. The SONOSim3D simulator system and the user interface of the simulator [12]. 20

Figure 2.14. The pipeline and the simulator environment for the work [13]. . . 21

Figure 2.15. The simulation output of the CT slice with the US image in the middle [14]. 22

Figure 2.16. From left to right: a CT slice of an oblique plane, the scattering image, the blended-simulated image [15]. 23

Figure 2.17. The simulation outputs: (a) from directly CT volume [16] and (b) from MRI data [17]. 23

Figure 3.1. The CT slices as a mock-up human body [18]. 25

Figure 3.2. The CT-to-density transformation function [19]. 26

Figure 3.3. The sampling process (Image courtesy of A. Karamalis). 27

Figure 3.4. The figure reflection and transmission mechanisms. 29

Figure 3.5. Sample reflection and transmission scanline images. 29

Figure 3.6. The US image and the results of Rice fit applied to it. 31

Figure 3.7. The speckle energy is empirically modeled by an US frequency dependent Rayleigh-like function of local entropy, $g(E; f)$. 33

Figure 3.8. The figure shows (a) a CT slice and (b) the map constructed based on its local entropy. 34

Figure 3.9. The figure shows a pair of CT (a) and US (b). The image (c) is the simulated output of the CT slice (b) with the scale parameters extracted from the US (b) data using the Rician fitting. 36

Figure 3.10. The effect of logarithmic scaling. 37

Figure 3.11. The effects of attenuation gain and supression of shadowing. . . . 37

Figure 3.12. Input CT image and corresponding reflection-transmission images with suppressed shadowing. 38

Figure 3.13. The multi-ray image formation geometry is composed of $2N+1$ rays per T transducers. Each transducer has a major view direction, $\mathbf{r}_{t0}$ and a field of view of 2θ, symmetric around $\mathbf{r}_{t0}$. Each pixel gets a contribution from all $T \times (2N + 1)$ rays. 38

Figure 3.14. The CT slice and the simulated image with 13 multirays and the parameters $f = 5MHz$, γ =2.54°. 39

Figure 4.1. The figure shows (a) The input CT, (b) The simulated output with $\sigma = 0$ and shadowing supressed, (c) The simulated image with speckle based on local entropy and shadowing supressed, (d) The simulated output with $\sigma = 0$, (e) The simulated output with speckle based on local entropy. 40

Figure 4.2. The effects of f, γ, N are depicted. (a),(b),(c) have shadow suppression while (d) does not. Increasing γ (decreased focusing) increased blurring for all cases. Increasing f changed the attenuation behaviour, esp. when the simulated speckle is added (d). Increasing N did not have much effect on simulated images. 42

Figure 4.3. The figure shows (a) The CT slice of one of the pairs,also used for input for the simulation, (b) The US image of the pair, (c) The simulated image with the estimated scale parameters. 43

LIST OF TABLES

Table 1.1. Comparison of Imaging Modalities [3]. 2

Table 2.1. Acoustic Properties of Some Materials. 6

LIST OF SYMBOLS

f	Transducer frequency
E	Local entropy
N	Number of transducer elements
R	Reflection image
RC	Reflection coefficient
S	Simulated signal
T	Transmission image
Z	Acoustic impedance
W	Window size
α	Angle between rays and query point
β	Logarithmic scaling variable
γ	Weighting factor
θ	Field of view angle
λ	Wavelength of ultrasonic wave
μ	Attenuation factor
σ	Speckle scaling parameter

LIST OF ACRONYMS/ABBREVIATIONS

1D	One Dimensional
2D	Two Dimensional
3D	Three Dimensional
CT	Computed Tomography
DR	Dynamic Range
FOV	Field of View
MRI	Magnetic Resonance Imaging
TGC	Time Gain Compensation
US	Ultrasound

1. INTRODUCTION

Medical ultrasound (US) is a technique which employs sound waves to image tissue in a noninvasive way. In the imaging process, a sound pulse is transmitted through human tissue with a device called transducer. As the sound pulse propagates through the tissue, it encounters with scatterers with changing densities and sizes. During this journey, while a fraction of the sound is exhausted due to converting its energy to heat in a friction like process, remaining part is reflected back to the transducer. These reflected signals, after processed in cascadading mechanisms, form the image to be seen and investigated by the end user, sonographers or doctors. All of these mechanism, acquiring the images, occur in miliseconds. The Figure 1.1 both shows the image of the human liver tissue which is acquired with a transducer operating at 5 MHz and the transducer utilized in the acquiring process. Compared to other modalities, medical

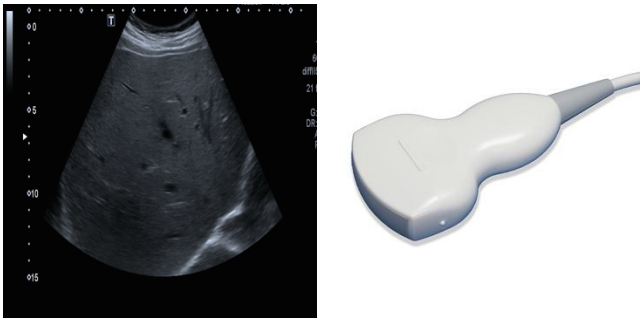

(a) (b)

Figure 1.1. The figure (a) is the US image of the liver acquired with the curved transducer Toshiba Aplio 500. The figure (b) is the transducer employed in the process [1].

US is commonly used in hospitals thanks to being low-cost and more compact. While it is one of the safest imaging systems since it neither employs ionizing radiation nor penetrates through the body (except some practices using needles), the system has a quite better spatial resolution with respect to other modalities. The Table 1.1 gives a quantitative comparison of the modalities. As can be figured out, the portability, safety, cost, and spatial resolution make medical ultrasound ubiquitously used in the medical

Table 1.1. Comparison of Imaging Modalities [3].

Modality	**Ultrasound**	**CT**	**MRI**
What is imaged	Mechanical Properties	Tissue Absorption	Biochemistry (T1 and T2)
Spatial resolution	0.3 - 3 mm	∼1 mm	∼1 mm
Penetration	3 - 25 cm	Excellent	Excellent
Safety	Very good	Ionizing radiation	Very good
Speed	100 frames/sec	Minutes	10 frames/sec
Cost	$	$$$$	$$$$$$$$
Portability	Excellent	Poor	Poor

sector. Despite of such advantages over the other imaging systems, the interpretation of ultrasound (US) images poses unique challenges due to its noise content-artifacts lowering its image quality, and view dependence and smaller field of view. Hence, the education of new ultrasound technicians, or sonographers is a time consuming process and needs an expert supervision during this training. To reduce and ease this interpretation problem, various ultrasound simulators, using mannequins, have been developed in years. In this thesis, such an ultrasound simulator will be proposed in which computed tomography (CT) images are used as priors. Before passing through the outline of the thesis, here is a good place to mention CT as an imaging modality since its images will be benefited to simulate US images in this thesis.

In computed tomograhy, X-rays are employed in which the rays are transmitted through the body with different angles producing tomographic images and then the tomographic images are computationally processed and combined to obtain a final image. Different than medical ultrasound, CT utilizes transmitted signals attenuated through the tissue to construct images. It creates high quality images of bones, lungs, soft tissue in a spatial resolution roughly about 1 mm. The main drawback of CT is that ionizing radiation - the energy range of the rays are about keV whereas radiations with energies higher than 13.6 eV is enough to ionize tissue - is utilized in acquiring process, which has a probability to cause cancer in patients. The CT machines are very bulky (see Figure 1.2) and expensive compared to ultrasound imaging systems.
After mentioning US and other modalities briefly above, the outline of further chapters

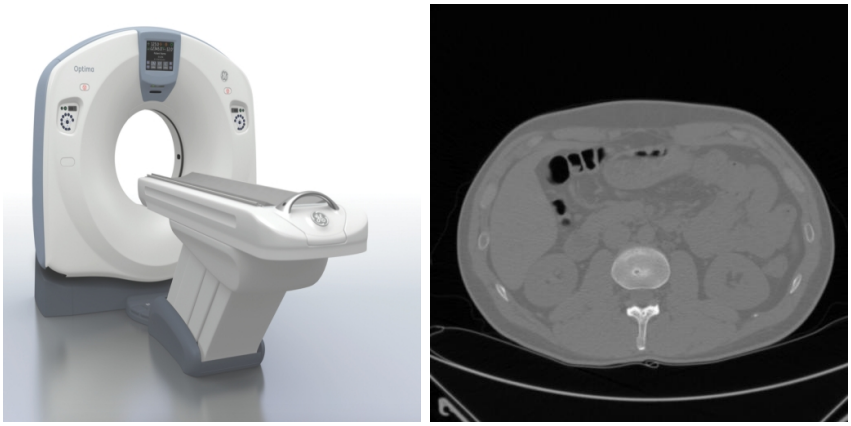

(a) (b)

Figure 1.2. The figure (a) shows a CT machine [2] and the figure (b) is an abdominal CT image.

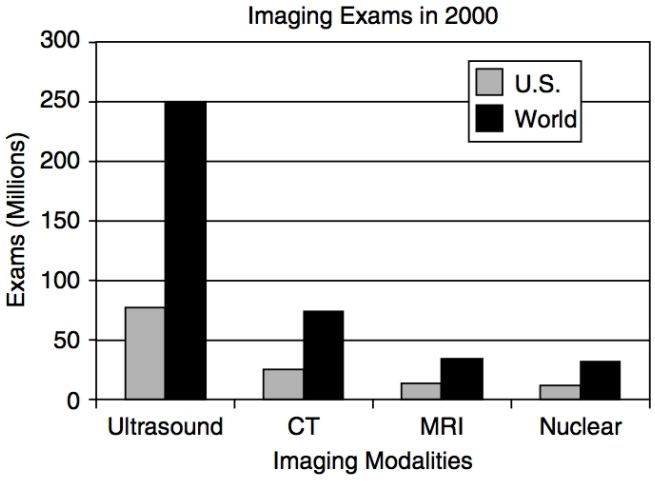

Figure 1.3. Estimated imaging exams taken in the U.S. and the World in the year 2000 [3].

in the thesis will be as follows:

(i) In Chapter 2, an ultrasound background will be given in a nutshell in which the physics of the sound waves, the ultrasound imaging system and a state-of-the-art of ultrasound simulators briefly. The physics and the imaging system of the ultrasound has been mainly gathered and summarized from the books by Cobbold [20] and Szabo [3].

(ii) In Chapter 3, a CT based ultrasound simulation will be detailed, which is studied and proposed in this thesis.

(iii) In Chapter 4, based on the methods described in the Chapter 3, various experiments and consequent results will be given with several images.

(iv) In the last chapter, considering the results and other works studied in the literature of ultrasound simulators, the thesis will be concluded.

2. ULTRASOUND BACKGROUND: PHYSICS, IMAGING, SIMULATIONS

2.1. Ultrasound Physics

Ultrasound is a sound (pressure) wave, whose frequency is over 20 kHz whereas audible sounds' frequency range is roughly between 20 Hz and 20 kHz. Medical ultrasound utilizes ultrasonic waves in frequency range between 1-10 MHz depending on the purpose of the imaging and the tissue to be imaged in the session.

Wave nature of sound should be investigated by looking into its physical changes, situations in different environments to go further. Hence, in this section, the fundamental laws governing the path of sound, such as how it is reflected, refracted, etc., will be introduced.

2.1.1. Sound Waves

Different from electromagnetic waves, sound waves need a medium in which it can propagate. The propagation process occurs with rarefaction and compression of medium by the wave. In other words, the wave compresses the medium and releases it to propagate. This dependency on the medium determines the speed of sound c, as written below:

$$c = \frac{1}{\sqrt{\kappa\rho}} \tag{2.1}$$

where ρ is the density of the medium and κ is the compressibility factor of the medium. As the equation suggests, the sound is faster in solids compared to gaseous media such as air (see Table 2.1). The way sound propagates is also a specification of sound wave. If its propagation is perpendicular to the particle displacement, it is called as a transverse wave whereas the mode where the both are parallel is called a longitudinal

Table 2.1. Acoustic Properties of Some Materials.

Materials	Density, ρ [kg m^{-3}]	Speed, c [m s^{-1}]	Characteristic Impedance, Z [kg m^{-2} MHz]	Attenuation Coefficient [dB cm^{-1}] (at 1 MHz)
Air	1.2	330	0.0004	12
Water	1000	1480	1.5	0.0022
Blood	1060	1570	1.62	0.15
Bone	1380-1810	4080	3.75-7.38	14.2-25.2
Fat	920	1450	1.35	0.63
Liver	1060	1570	1.64-1.68	1.2
Muscle	1070	1600	1.65-1.74	0.96-1.4

one. In medical US, mainly longitudinal sound waves are used.

2.1.2. Wave In Media

The mechanisms governing the path of the wave in medium can be categorized by cases of the wave's wavelength with respect to medium/particle's size.

When a wave faces a medium whose interface is larger than the wave's wavelength, specular reflection process is observed, where the wave is reflected, refracted and transmitted (see Figure 2.1). Before showing some calculations of this mechanism, the crucial parameter, characteristic acoustic impedance Z, should be defined. The relation is given by

$$Z = \rho c \tag{2.2}$$

where ρ and c are density of the medium and the speed of sound in the medium respectively. This parameter is used in calculations of how much the wave is reflected, transmitted and how much it is refracted. Exploiting the Snell's Law, these coefficients and the relation for refraction can be found by

$$RC = (\frac{Z_2 \cos\theta_i - Z_1 \cos\theta_t}{Z_2 \cos\theta_i + Z_1 \cos\theta_t})^2 \tag{2.3}$$

$$T_c = \frac{4Z_1 Z_2 \cos^2\theta_i}{(Z_2 \cos\theta_i + Z_1 \cos\theta_t)^2} \tag{2.4}$$

$$\sin\theta_t = \frac{c_2 \sin\theta_i}{c_1} \tag{2.5}$$

where c_1 and c_2 are the speeds of sound in medium 1 and medium 2 respectively. If wave

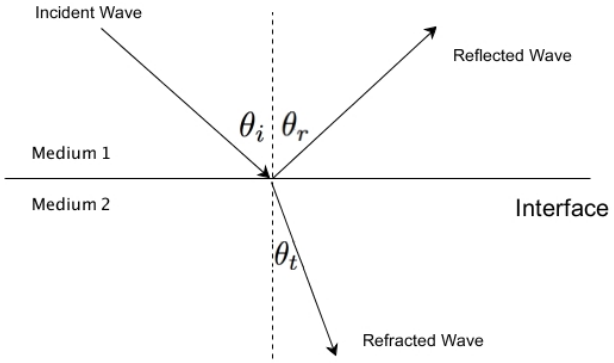

Figure 2.1. Wave encountering with a different medium larger than its wavelength.

faces a smaller interface, say a smaller particle, than its wavelength, then scattering takes place. In this case, it is not easy to write such equations like above. In general, it can be thought as diffuse reflection where the wave is scattered all around.

Attenuation is one of the main mechanisms for losing energy for waves propagating in media. It is mainly due to very smaller particles in medium, which converts the wave's energy to heat. Attenuation coefficients also differ from medium to medium. The important fact in here is that attenuation coefficients are usually linearly increasing with frequency of the wave. The Figure 2.2 illustrates the increasing attenuation

with a higher frequency sound pulse. As frequency increases, the structures in deeper areas degrade and have less brightness. Last but not least, the interference is the mech-



Figure 2.2. The figure left is the image of the liver obtained with a transducer at 4 MHz while on the right one is the image of the same liver portion acquired with a transducer operating at 6 MHz [4].

anism, as stays for all wave types, in which waves interact with each other, resulting in reinforcement and cancellation, or construction and destruction of them. As will be investigated in more details in further sections, the constructive and destructive interfererences are the reasons for speckle to exist in ultrasound images.

2.2. Ultrasound Imaging

The medical ultrasound systems, that are used today, date back to 1963. Though their size, display quality, working speed have changed and developed up to this time, the main working principle to form an image does not change. This image formation is known as pulse-echo imaging, in which an ultrasonic wave pulse is transmitted and echoes reflected from tissues are acquired. Mainly, the algorithm works as follows:

(i) The position of the tissue to be imaged is determined by transforming time signal

to space information, which is given by the relation

$$d = ct/2 \tag{2.6}$$

where d is the position of the tissue, t is the time between signal is transmitted and received.

(ii) The brightness of the signal to be written on the image for that tissue is assigned from the intensity received at the time tissue is positioned.

The Figure 2.3 illustrates the pulse-echo imaging algorithm briefly written above. In the subsections below, transducers, image formation and image specifications will be mentioned.

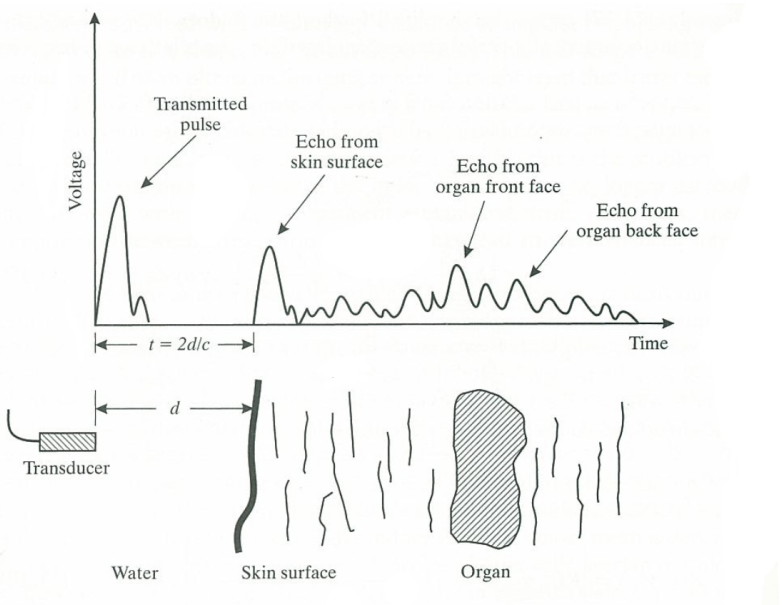

Figure 2.3. The process of acquiring A-mode signal [5].

2.2.1. Transducers

Transducers, which are inevitable components of ultrasound imaging systems, both transmit ultrasonic pulse and receive echoes reflected by tissue. Transducers owe their being both transmitters and receivers to piezoelectric materials. The material inside transducer elements have the speciality that when a voltage applied to it, a sound wave is generated and when a sound wave received by the material, it converts pressure to voltage.

Transducers are mainly categorized into three as convex, linear and phased array ones (see Figure 2.4). Linear and convex transducers are basically have the same working principle, but the latter ones have wider field of view as their geometry suggests. On other hand, phased array transducers have elements whose firing can be contolled by user which enables steering.



Figure 2.4. Types of transducers [6].

2.2.2. Imaging Modes

Ultrasound modality can acquire signals in various modes. The important ones are A-mode, B-mode, M-mode and Doppler mode.

A-mode, illustrated also in Figure 2.3, is simply the amplitude (intensity) versus time signal of a single pulse fired by one transducer element. It is used especially in length measurements, e.g. to measure the size of eye ball.

In M-mode, where the letter M stands for motion, sonographers want to detect

motion for example, whether there is an arrhythmia in a patient, which is a problem with the rhythm or rate of the heartbeat. M-mode is a time evolved version of A-mode signal acquired always from the same line.

Brightness mode, or B-mode signal is designed for scanning a 2D tissue of interest with firing from more than one element. Lines scanning the tissue space are actually A-mode signals; but rather than amplitudes, gray scaled values are used to form the final image. In the Figure 2.5, the upper fan shaped image is a B-mode image of mitral valve and the one below is the time evolved signal image of the dotted line in the fan shaped one. Lastly, Doppler ultrasonography is based on the Doppler effect, which

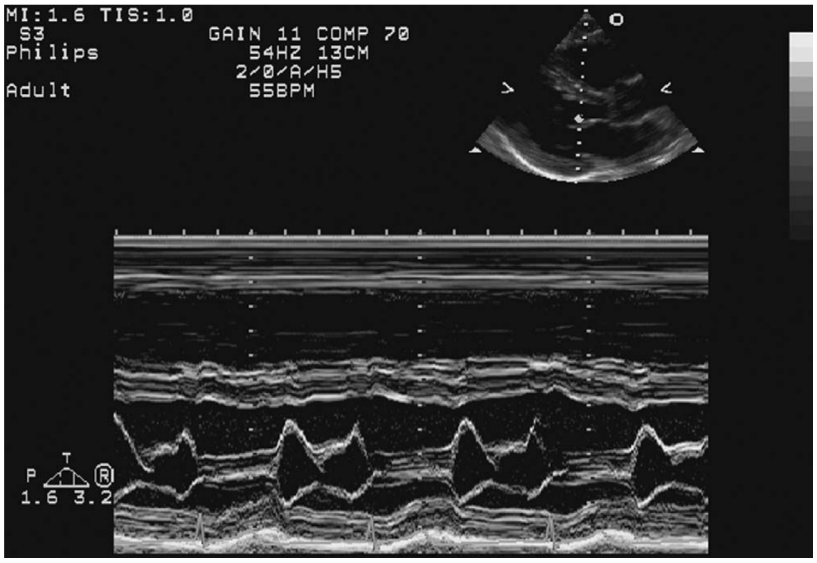

Figure 2.5. B-mode (upper right) image and M-mode signal (below) of the mitral valve [3].

is the change in frequency of the wave reflected from moving tissue. The Figure 2.6 shows a color Doppler US image of blood flowing through a normal artery (red) and vein (blue).

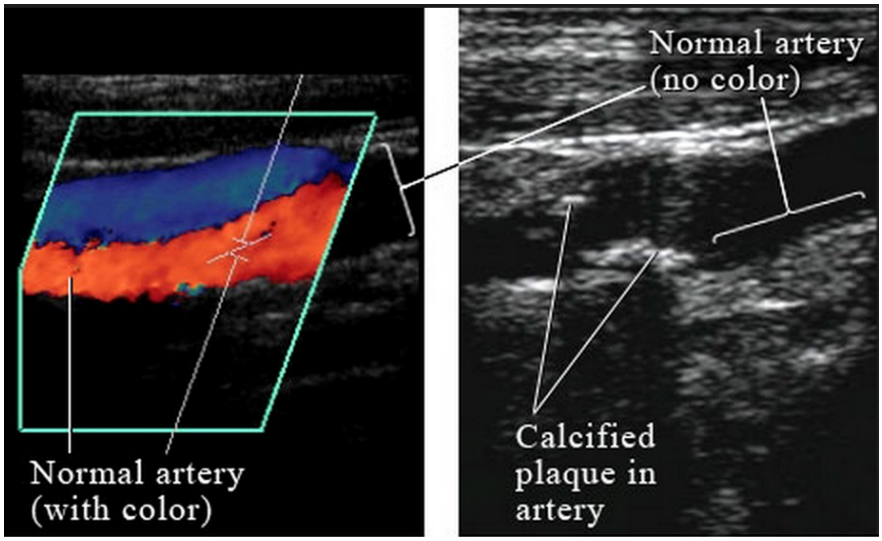

Figure 2.6. The image left is color coded Doppler US on top of B-mode image which stays on right side [7].

2.2.3. Beamforming and Postprocessing

After pulse goes through tissue and come back to transducer, a few procedures are applied to form final image on the display. First of all, it is required to know that, typically the output signal of an ultrasound system is the envelope not the signal as transducer elements generated. After extracting envelopes of the signals received by the elements, the envelopes of transducers are shifted according to their distance to points to be imaged in tissue. The delays are configured such that at the end, all scan lines are simply summed to assign a value to the target point in the image. The process is depicted in the Figure 2.7. As mentioned in the subsection above, phased array transducers can steer beam electronically by firing each transducer at different delay times. In other words, phased array transducers can be used to focus on a point of interest in transmission mode as in the situation of beamforming written above. As seen in Figure 2.8, each transducer element has its own delay time to send a pulse and all together form a focused beam to be scattered by the tissue at that focal point. Since the more ultrasonic pulse propagates the more it loses its energy due to attenuation, an exponential-like compensation function, called as time gain compensation (TGC),

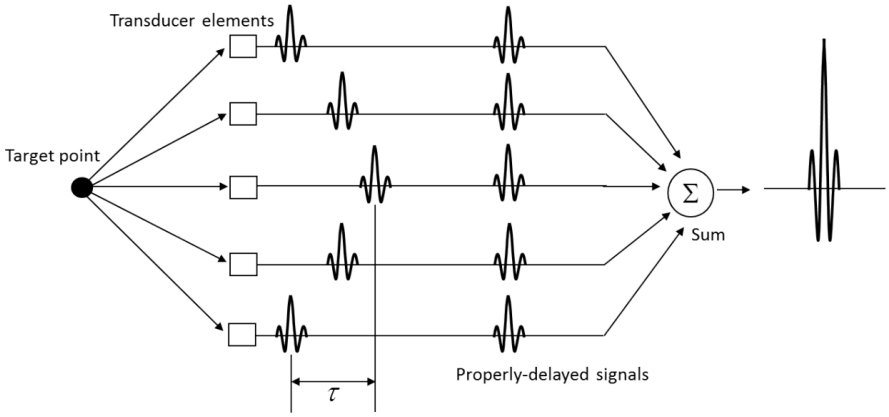

Figure 2.7. The mechanism of beamforming based on calculation of delays τ of each element [8].

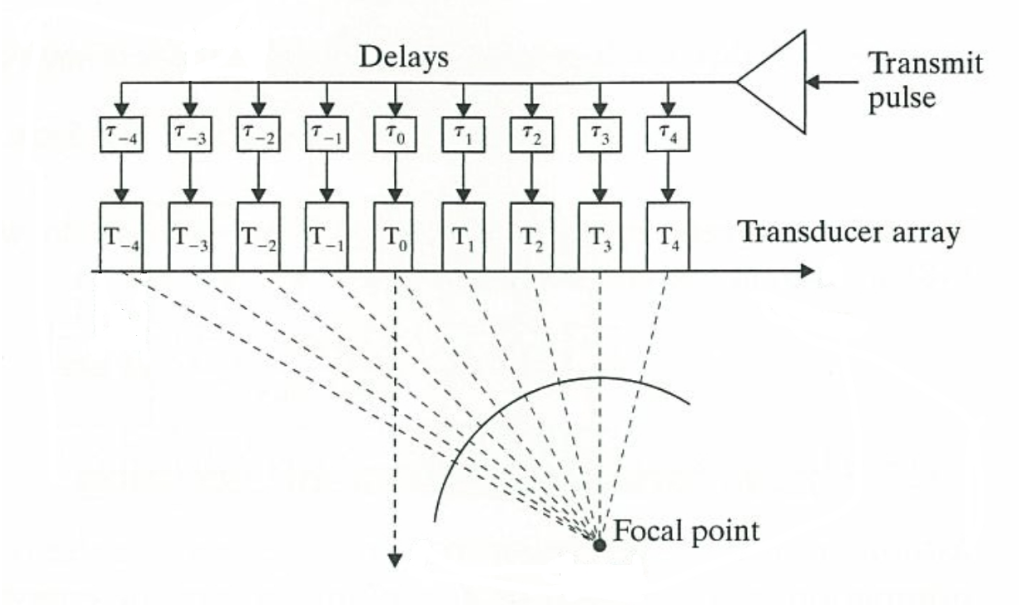

Figure 2.8. The firing mechanism of phased array transducers [5].

is practiced to circumvent this problem. Also a total gain control is available for sonographers to amplify the echo signals.

Such processed bare signals are not appropriately seen and differentiated by human eye. Hence, a process called Dynamic Range (DR) is applied to the signal which scales the interval between the strongest and weakest ones usually with logarithmic scaling.

As the last step, scan conversion is applied to give a fan shape to the image. It is the process in which the lines are interpolated to form the 2D final image (see Figure 2.9).

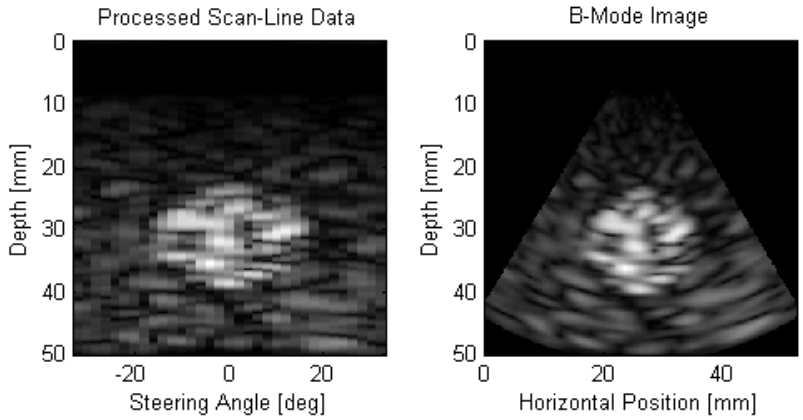

Figure 2.9. The scan conversion of scan lines [9].

2.2.4. Image Specifications

To give logical judgements about the output image from an ultrasound system, the physics behind the mechanisms and which assumptions are made should be known. The artifacts and speckle reveal themselves in this phase.

There are a few assumptions to construct images using the ultrasound:

(i) sound wave propagates at a constant speed of 1540 m/s
(ii) the pulses are directly transmitted to the reflectors and directly received by transducers
(iii) echo strength is directly corresponds to reflection strength of a scatterer

These assumptions lead to erroneous positions of scatterers, improper brightness value and even unreal structures in images. Artifacts, that are basically results of the assumptions made, are the structures and features constructed in the algorithm of the imaging modality, which is expected to reveal what is happening in the tissue investigated. As it is mentioned above, the structures in the tissue and in the corresponding image are not one-to-one.

Some of the frequently faced artifact examples are shown in the Figure 2.10. Reverberation artifact occurs when sound propagates through two parallel strong reflectors. The wave reflects back and forth between them in a periodic fashion. Mirror images are seen in the image if a reflector and a strong interface like diaphragm below it exist. While the reflector's true position is assigned to the image, another reflector located to twice the distance between the reflector and the interface is positioned due to bouncing of the wave between the interface and the reflector. Another artifact is shadowing in which no sound energy goes behind a structure. These structures have a high acoustic impedance and as Equation 2.3 suggests that if the sound wave propagating in a low medium encounters with a medium of high acoustic impedance, the intensity of the transmitted wave is significantly decreased (or vice versa), hence shadowing occurs. The air-liver or bone-muscle interfaces are examples of the artifacts. Speckle, one of the important image characteristics, is the granular and dotted texture in ultrasound images. When an ultrasonic pulse progapagates through medium, it encounters with tiny particles that are not resolvable. These unresolvable particles respond to the wave in an interference mechanism in which all of them result in either a constructive or destructive way. From this aspect, it seems speckle is a noisy texture in ultrasound images, however it has a deterministic nature also. When the tissue is reimaged by the

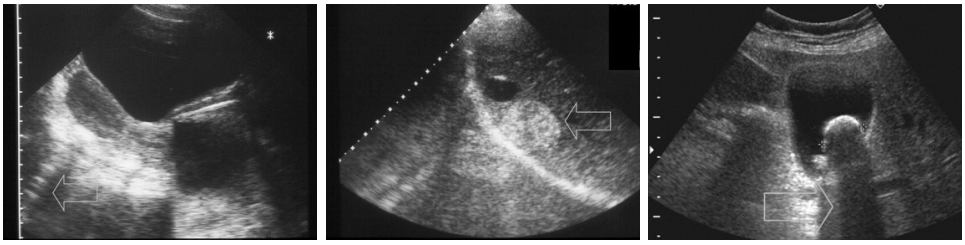

(a) Reverberation (b) Mirror (c) Shadowing

Figure 2.10. Some of the artifacts [10].

same system parameters (the same field of view, operating frequency, etc.), the image seen on the display will be again almost the same image acquired before. Hence, it can be said that, speckle has both noisy and deterministic nature.

Some of the typical characteristics are marked in the Figure 2.11.

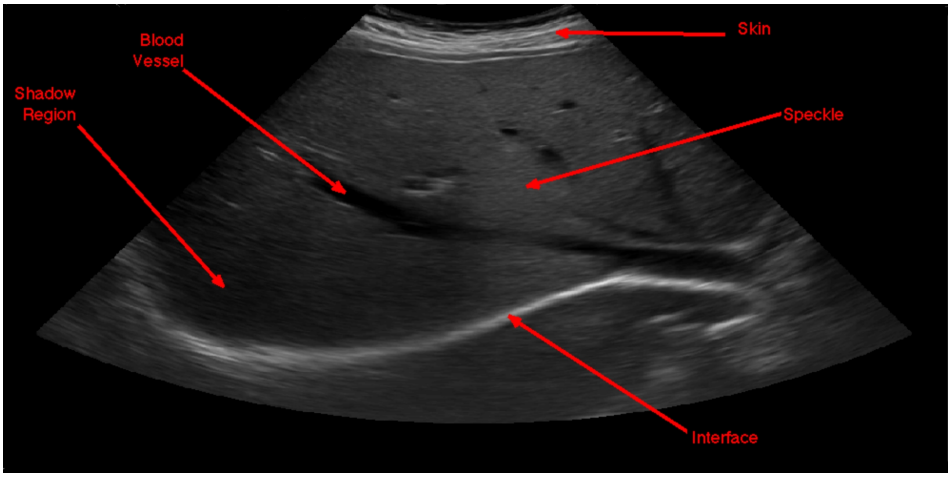

Figure 2.11. Some of the characteristics in usual US images.

2.3. Ultrasound Simulations

As mentioned before, ultrasound simulators are aimed:

(i) to make new designs or optimize ultrasound systems,
(ii) register ultrasound with different modalities like with CT,
(iii) to produce a training setup.

Hence depending on the purpose of the simulator, the requirements for the speed/load issues of the working flow may change from one to another. The second and third purposes, especially the ones for training goals, need a real-time working algorithms. The first one, on the other hand, sets no limit to the computational time.

The need for solving the physics behind the system with a high accuracy for simulators of the first group loads a heavy computational cost. Such simulators are performing in hours to give results. The most well-known simulator in this group is Field II [21]. It solves the spatial impulse response of propagating and received wave for a given volume distribution of scatterers. In spite of the realistic view and high accuracy, its computational load is very high such that with a cluster of computers, the simulation lasts up to 10 hours.

Real-time simulators with training purposes needing real-time working algorithms might be divided into two as interpolative and generative methods. In principle, they are lacking realism and accuracy with respect to wave based methods, but their high speed and low computational task make them attractive. The realism factors in that simulators are virtually tried to be implemented by adding/blending/convolving some images to give realistic view to outputs.

2.3.1. Interpolative Methods

The interpolative methods use pre-recorded real US image volumes. This type of simulators track the virtual/real probe position and orientation, determines the US image plane, extracts a 2D cross-section by interpolation. The interpolated US image is virtually realistic since the images are extracted by real US images.

The UltraSim system studied by Aiger *et al.* [11], consists of a dummy ultrasound

imaging system, a dummy transducer and a plastic mannequin. Measuring the position and angle of the transducer, the system displays a 2D US image on display. The correct slice is found by correlating the position with the pre-recorded 3D US volume by extracting the interpolated slice. In the Figure 2.12, the mock-up imaging system with the dummy transducer and mannequin and the user interface of the system is placed. SONOSim3D proposed by Ehricke [12] is also based on a digital patient model, a graphical computer and a visualization software. Different from UltraSim, in this method, to help trainers for easing the anatomic interpretation of displayed images, there exist different modes of the output images (i.e, CT, MRI) with which trainers may switch between. Also various cases and transducer models are presented to train in different setups. The slice to be shown on the display is again selected by registering the mock-up transducer's position and the reconstructed slice within the prerecorded 3D US volume. The Figure 2.13 shows the working elements of the system and the user interface of the training module. Using the finite element method, Goksel *et al.* [13] suggest an ultrasound simulator for a synthetic tissue phantom. In their work, they again use 3D US volume, but depending on the probe's position and/or the situation of inserting a needle, they deform the volume and extract the corresponding US slice by interpolating it taking account these effects. This tecnique is integrated to a haptic simulation to use it as a probe, give the user a force feedback as if pressing the transducer through the body or the surface of the model. In the Figure 2.14, the pipeline and the hardware-software environment of the simulator is placed. In the interpolative methods, unless the simulator's probe position and orientation do not coincide with the US probe position and orientation during recording, the simulated image does not correspond to any real US image. This often ignored problem is mostly observed as unrealistic shadowing and attenuation effects.

2.3.2. Generative Methods

The generative methods are based on models of the underlying physical phenomena. There are two major approaches: wave-based and ray-based methods.

The wave-based methods solve the wave equation for an acoustic wave prop-

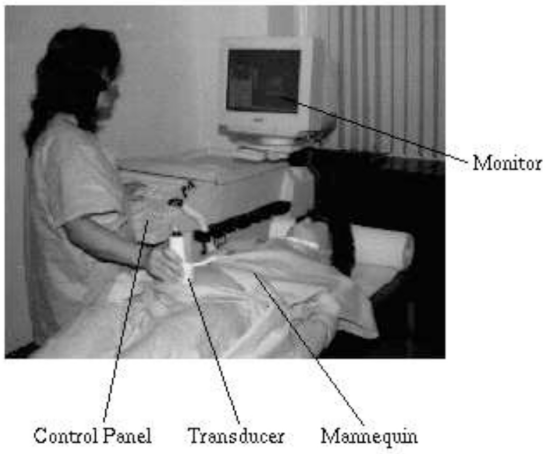

(a)

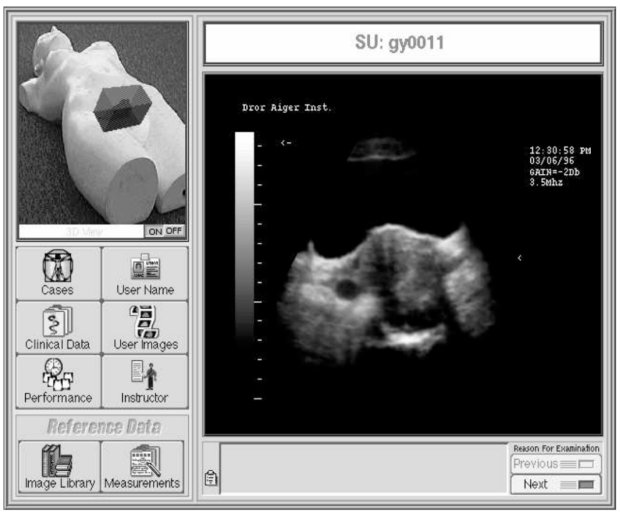

(b)

Figure 2.12. The UltraSim simulator system and the user interface of the simulator [11].

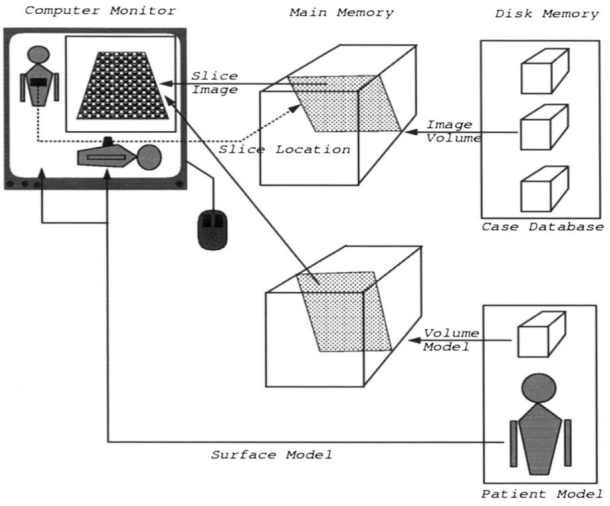

(a)

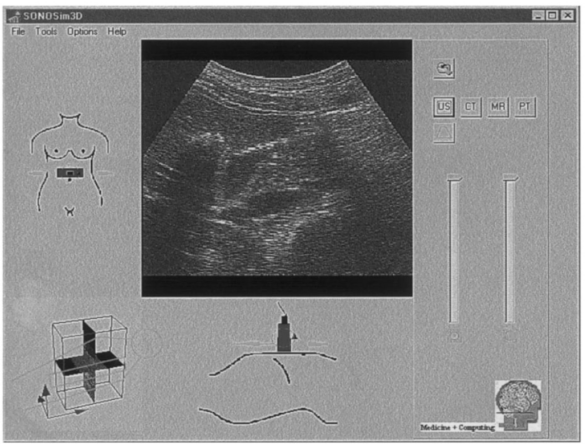

(b)

Figure 2.13. The SONOSim3D simulator system and the user interface of the simulator [12].

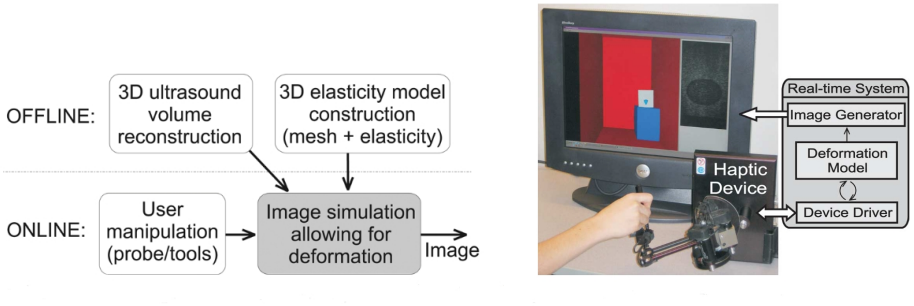

(a) (b)

Figure 2.14. The pipeline and the simulator environment for the work [13].

agating in the imaged domain. As mentioned in the section above, Field II is the most famous simulator among this kind of solvers. The drawback of these methods is the incapability of working real-time though they are physically more accurate than ray-based ones.

The ray-based methods follow the principles of ray optics. Firstly, a domain is constructed from a modality like CT, MRI, etc., or a volume is modeled as a phantom similar to a part of an organ and its enviroment. Then, with the position of the transducer measured, the interested slice is generated utilizing a ray tracing method which is suitable to sound rays. In usual, the calculations contain only reflection and transmission which are produced by tracing the rays. Hence the computational time is significantly reduced concerning the wave-based methods described above. They are suitable to real-time implementation, especially with GPU, which usually have a frame rate over 10 Hz.

In their work, Wein *et al.* [14] propose a simulation for registering CT and US images automatically, in which a ray tracing method is employed. Depending on the geometry of the transducer used, a slice within a CT volume is processed. After sampling the pixels, the CT Hounsfields units of them are mapped to the acoustic impedance values with the help of a function found by a study of Schneider and his collaboraters [19]. By finding the acoustic impedance values, as stated in Equation 2.3, the reflection coefficients and consequently reflection and transmission values are

calculated in the ray-casting scheme which will be detailed in further sections. The typical characteristics in US, shadowing and reflection are simulated in a good quality. For realism concerns, Perlin noise is added to the output images. The Figure 2.15 contains the CT (a) and US (b) images of the same region and the simulated US image (c) generated from the CT slice. In the works by Shams *et al.* [15] and Kutter *et al.* [22],

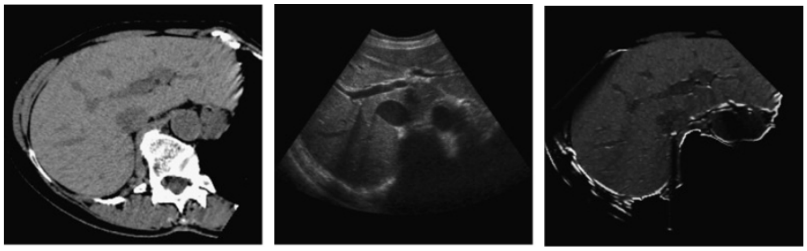

(a) CT (b) US (c) The simulated output

Figure 2.15. The simulation output of the CT slice with the US image in the middle [14].

the function mapping the CT units to acoustic impedance values is benefited as in the study by Wein. A fixed scattering volume is generated from the CT volume by the help of the program Field II, which is acuired before the simulation. After acquiring these prerecorded scattering images, the ray racing method is employed to obtain reflection images Finally they are blended with a weighting selected by the user and post-processed with a logarithmic function to handle dynamic range issues. To enhance the computational performance of the algorithm, Kutter, differently, implement the steps in GPU. The Figure 2.16 shows a CT slice, the corresponding scattering image and the final image. In the study of Hostettler *et al.* [16], the volumetric ray tracing is applied directly to the CT slice which gives the reflection image. Also from CT image, the absorption map is extracted by labeling pixels as bones, soft tissue, air, etc., which represents the acoustic properties of the slice. Finally the simulated image is obtained by merging these images. Wenjian *et al.* [17], on the other hand, apply the ray-casting method utilizing 3D MRI data. The pixels, then, are labeled as bone, air, fat, and blood by manual segmentation and from these labels, the acoustic parameters are gained. As the last step, the reflection, transmission and a speckle pattern following Rayleigh distribution is combined. In general, generative approaches have the advantage of being

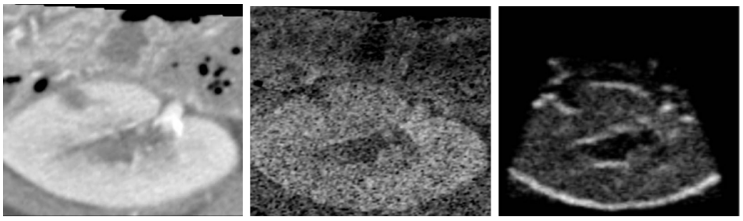

Figure 2.16. From left to right: a CT slice of an oblique plane, the scattering image, the blended-simulated image [15].

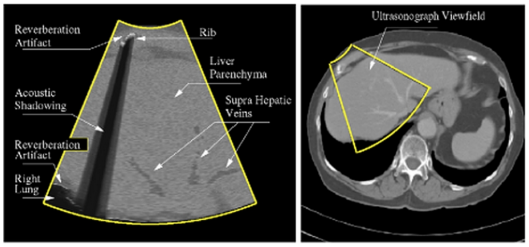

(a) Hostettler's simulation result

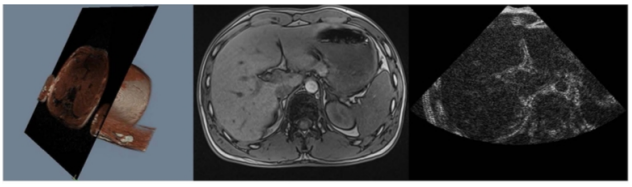

(b) Wenjian's simulation result

Figure 2.17. The simulation outputs: (a) from directly CT volume [16] and (b) from MRI data [17].

applicable to any type of organs provided that a model of them is available. However, as it is mentioned above, the acoustic phenomena to be rendered are extremely complex and even simplified simulation is very time-consuming. As a result, a compromise between ray-based methods and wave-based methods is desired, with which a higher physical accuracy and higher frame rates can be acquired.

3. CT BASED ULTRASOUND SIMULATION

In this chapter, the real-time working ultrasound simulation based on the ray-based method using CT slices as priors will be presented. This work is aimed to provide realistic ultrasound outputs, which can be used with registration and/or real-time simulation purposes. Throughout this chapter, the method for single ray simulation and multiray beam formation will be detailed.

Before passing the simulation details, here, why CT datasets as priors are employed will be explained. Compared to other modalities, CT datasets can be more commonly obtainable from the databases of hospitals. Also, even if ultrasound datasets were available in the hospitals, they would not be easily used to make a simulation, since ultrasound outputs are acquired with a definite view and any change in the position of the transducer gives different results. This view dependency of US, makes it hard to use as simulation inputs. However, simulators employing CT volumes gives freedom to choose any viewing plane. With the facts that various patient cases available and the view is of no importance for CT, a computed tomography volume can be thought as a patient (see Figure 3.1) and the transducer is placed with any position and angle wished by trainers as if they are trying to diagnose a patient in an imaging session.

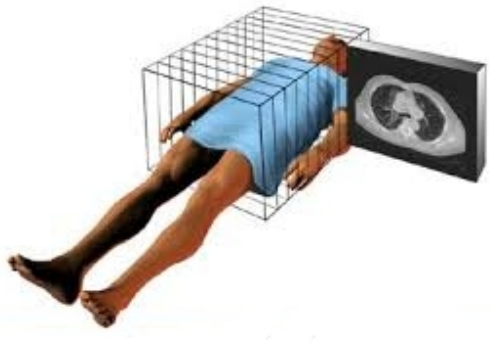

Figure 3.1. The CT slices as a mock-up human body [18].

3.1. Single Ray Method

Adapting the Wein *et al.* method [14], the single ray method for ray tracing algorithm, which is basically composed of the ray sampling, the domain modeling and the scan-ray simulation will be described in the further subsections.

3.1.1. Domain Modeling

To make calculations, a transformation from CT domain to acoustic impedance domain is required. There exists such a function which maps CT Hounsfield units to density, proposed by Schneider *et al.* [19]. As can be seen from the Figure 3.2, it is a piecewise function that maps CT units to density. The computation of the density based on the function is done with the help of k-Wave toolbox [23] Since density cannot

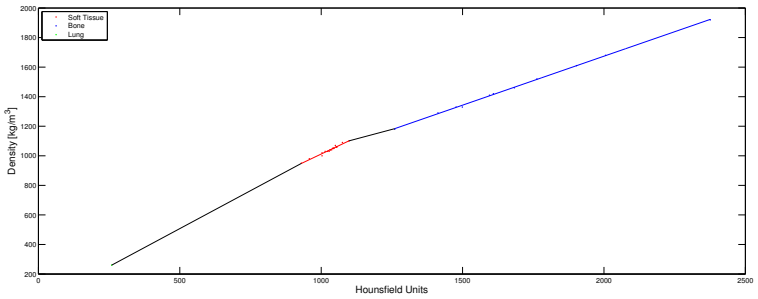

Figure 3.2. The CT-to-density transformation function [19].

be directly used, the mapped values are multiplied by the speed of sound, which is a assumed-constant of 1540 m/s, found from the relation $Z = \rho c$ given before.

3.1.2. Ray Sampling

After passing to ultrasound domain by transforming CT intensity values to acoustic impedance, Z values, rays to be emanated are calculated. A 2D oblique slice is extracted from the Z-volume, on the plane defined by the virtual US probe, with the probe positioned at the center of the in-contact edge. The determination of the plane

defined by the virtual probe depends on:

(i) the number of rays emanated from each transducer, N,
(ii) the field of view (FOV) spanned by rays,
(iii) the range of rays along the radial direction, L,
(iv) the sampling distance Δr determined by frequency of the probe, f.

While the 2D plane is spanned depending on the parameters, N, FOV and L defined by the user, the sampling distance is determined by the axial resolution of the ultrasonic pulse, which is typically the wavelength of the pulse, $\lambda = c/f$. So at each λ, samples of Z are obtained.

The Figure 3.3 illustrates the sampling process before the ray simulation.

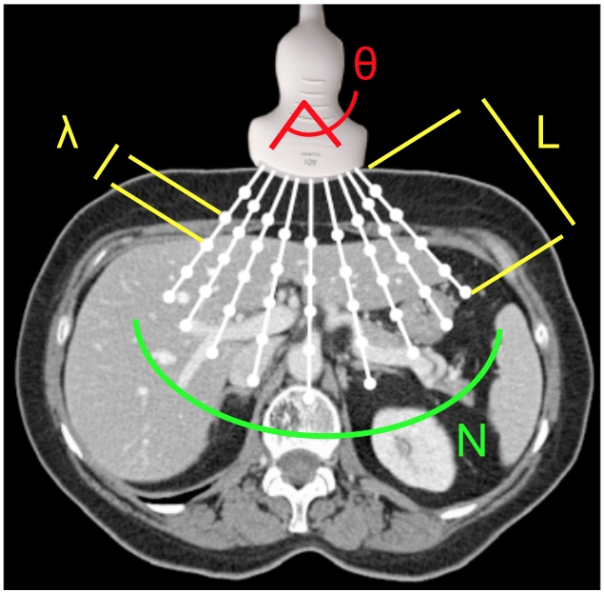

Figure 3.3. The sampling process (Image courtesy of A. Karamalis).

3.1.3. Ray Simulation

Knowing that acoustic rays reflect at acoustic impedance boundaries, the sampled Z values along the rays are used to compute reflection coefficients, RC and consequently, right after that to find the reflection, R and transmission T intensities.

As discussed before in the section related ultrasound physics, the reflection coefficients can be obtained by

$$RC_i = (\frac{Z_{i+1} - Z_{i-1}}{Z_{i+1} + Z_{i-1}})^2 \tag{3.1}$$

where, it is assumed that the rays are directly face boundaries, in other words, the angle between the ray direction and the boundary normal is always 0. From the equation, it can be said that to compute reflection coefficient at ith sample point, the pixels before and after are used.

After obtaining the coefficents, the reflection and transmission intensity values along the rays are computed in an iterative fashion. The steps in the ray simulation algorithm are implemented as follows:

(i) The transmitted signal is initialized with the value 1,

(ii) the reflected signal at the ith sampled point is found by Equation 3.2,

$$R_i = T_{i-1} \times RC_i \tag{3.2}$$

(iii) the remaining signal, the transmitted intensity for the next step is then defined by Equation 3.3,

$$T_i = (T_{i-1} - R_i) \times exp(-\alpha \times \mu \times \Delta r) \tag{3.3}$$

where μ is a pre-calculated value obtained by labeling CT images as bone, soft tissue and air, and α is a user-defined parameter. The exponential term in this

equation accounts for attenuation along the depth direction.

The reflection-transmission process mentioned in steps is depicted in the Figure 3.4. The calculations above are done for each ray and can be implemented independently

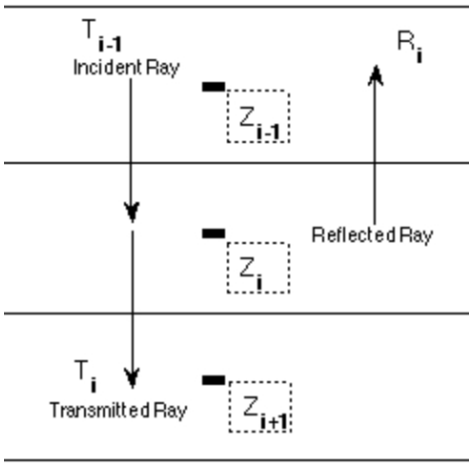

Figure 3.4. The figure reflection and transmission mechanisms.

from each other, which makes the algorithm paralelizable, therefore, makes the simulation a faster one. Sample scanline images of reflection and transmission are shown in the Figure 3.5. For training concerns, strong reflection coefficients (i.e, in air-tissue interfaces) are suppressed to disable shadowing in the images throughout the thesis.

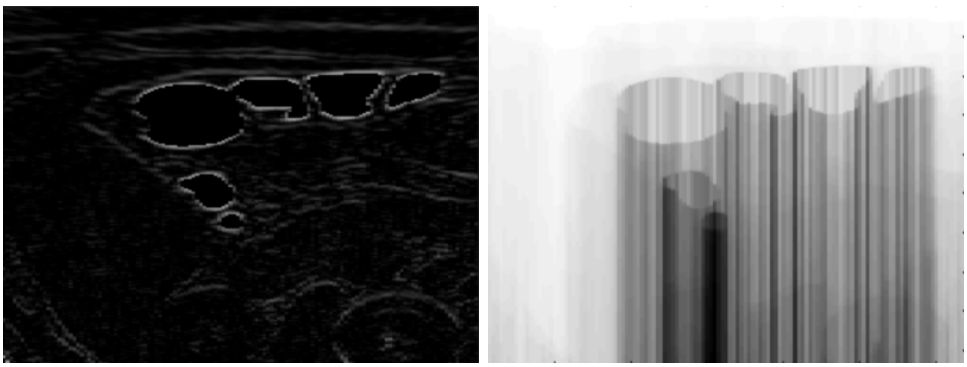

(a) Reflection Scan Lines (b) Transmission Scan Lines

Figure 3.5. Sample reflection and transmission scanline images.

3.2. Speckle Modeling

Optionally, right after the ray simulations are done, speckle is added to the simulations as will be described in further subsections below. This process adds texture to the simulation images before applying post-processing mechanisms. In the literature, there are various methods to achieve model speckle in ultrasound images. Usually a simple (Gaussian, Perlin) noise is added for compensating this factor in the literature.

Back to reality, previous works on ultrasound image speckle modeling report Rayleigh and Rician distributions, the Rician being a more general model [24, 25]. Assuming there is a large number of scatterers randomly distributed and occupying a tiny volume, speckle distribution can be found as follows. The complex signal received from that tiny scatterers can be denoted by phasors of the form Ae^{jwt}. The phase shifts are due to variations in positions of the scatterers. Also the real and imaginary parts of the phasor might be denoted by cosine and sine terms, known from Euler formula. If the number of scatterers is large and the phases are uniformly distributed, by Central Limit theorem, the real and imaginary parts of the phasors can be thought as Gaussian random variables. Since the amplitude of the signal is convenient to be used in ultrasound systems, the amplitude of the sum of the phasors follows the Rayleigh distribution. However, if a coherent reflector exists in that volume, it is mostly the case in ultrasound images, the distribution is given by Rician distribution. This distribution is specified by the following probability density function

$$Rice(s; v, \sigma) = \frac{s}{\sigma^2} exp\left(\frac{-(s^2 + v^2)}{2\sigma^2}\right) I_0\left(\frac{sv}{\sigma^2}\right) \tag{3.4}$$

where I_0 is the modified Bessel function, v is the complex valued non-centrality, σ is the real valued scale parameter and s represents the US envelope signal in this context. As $Rice(s; 0, \sigma) = Rayleigh(s; \sigma)$, v can be taken to represent the *structure*, which is the source of major acoustic reflection and hence is mainly probe position and view angle dependent.

Assuming the Rician distribution, the simulated US signal, S can be modeled

using two independent Gaussian distributed random variables, $\mathcal{X}$ and $\mathcal{Y}$, as

$$S = \sqrt{\mathcal{X}^2 + \mathcal{Y}^2} \ , \ \mathcal{X} \sim \mathcal{N}(\Re(A), \sigma^2) \ , \ \mathcal{Y} \sim \mathcal{N}(\Im(A), \sigma^2) \tag{3.5}$$

where A and σ are called the the complex valued non-centrality and the real valued scale parameters of the underlying Rician distribution, respectively.

Based on the assumption that the reflected acoustic energy, R_i, along a ray is the main image component for that position, for both models in the subsections below, A_i is set to equal to $R_i \in \Re$ for the ith pixel along the ray. The models, hence, are for finding the scale parameters, σ of that Gaussians.

A Rician fit is applied to a real US image (actually, envelope of the image will be desribed in detail in further sections) and the results are shown in the Figure 3.6. As can be seen from the figure, the model seems valid, since the v parameter map is clearly correlated with the high reflection regions, namely structures. For practical

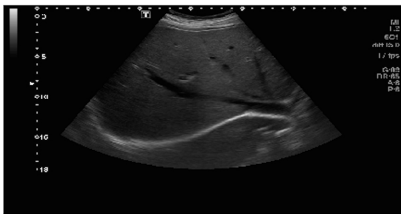

(a) A real B-mode US image



(b) The fitted σ parameters

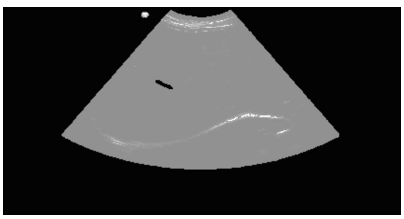

(c) The v parameters

Figure 3.6. The US image and the results of Rice fit applied to it.

reasons, here is a good place to change notation. Rather than using indexed notations, a ray, $\mathbf{r}$, is discretized with $\Delta r = 1540(m/s) \times f(MHz)$ and the sample point, r is set

to equal to $i \times \Delta r$.

With passing to the new notation, the 1D simulated US signal, $S(r)$, along a ray is described by two independent Gaussian random variables as

$$S(r) = \sqrt{\mathcal{X}^2(r) + \mathcal{Y}^2(r)}\ ,\ \mathcal{X}(r) \sim \mathcal{N}(R(r), \sigma^2(r))\ ,\ \mathcal{Y}(r) \sim \mathcal{N}(0, \sigma^2(r)) \tag{3.6}$$

In this thesis, two speckle model is employed: i) a method based on using local entropy feature of CT images, ii) a model based on machine learning algorithm, specifically k-Nearest Neighbors algorithm (k-NN), which trains CT and corresponding US data obtained from real patients and give a scale parameter in return.

3.2.1. Local Entropy Based Model

The local texture at the pixel i is quantified using the entropy of CT values, $E(r)$, computed locally over a window (of size $W = 15 \times 15 \times 15$). The entropy is a measure of inhomogeneity and is utilized as an approximation of local scatterer density. It is defined as

$$E(r) = -\sum_{j=1}^{D} P(j) \times log_2(P(j)) \tag{3.7}$$

where D is the number of discreete CT values in the window W around the point r and $P(j)$ is the frequency of occurrence of the jth CT value in that window.

After introducing the local entropy, the scale parameter for the point r is modeled deterministically as

$$\sigma(r) = g(E(r); f) \times T(t) \times \sqrt{RC(r)} \tag{3.8}$$

As known, speckle is physically dependent on frequency, scatterer size, scatterer density distribution and the acoustic power. $(T(r)\sqrt{RC(r)})$ dependence relates the speckle en-

ergy to the received acoustic power, essentially suppressing the signal at low reflecting homogeneous regions and/or regions under shadow. The scatterer density and size distribution is modeled by the local entropy, E. The frequency and scatterer distribution of σ is modeled by a frequency dependent Rayleigh-like function of local entropy, as in Equation 3.9.

$$g(E(r);f) = \begin{cases} 0.05 & , E(r) < 0.2\lambda \\ \frac{1}{K}(\frac{E(r)-0.2\lambda}{0.0004f^2} \times exp(\frac{(E(r)-0.2\lambda)^2}{0.08f^2})) + 0.05 & , \text{o.w.} \end{cases} \tag{3.9}$$

where $\lambda = \frac{c}{f}$ and K is the normalizing constant such that $max(g(E(r);f)) = 1$.

Figure 3.7 depicts $g(E(r);f)$ as E and f varies. Scattering energy would be maximal when the scatterer size matches the acoustic wavelength in scale. It would also increase with increasing reflectivity of the scattering surface and scatterer density. The local entropy, on the other hand, would increase with increasing scatterer density or decreasing scatterer size. Hence, we may expect to have an optimal entropy range that would maximise speckle for a given acoustic signal frequency, and to have this window shift to higher entropy values for higher frequencies. The Figure 3.8 shows a

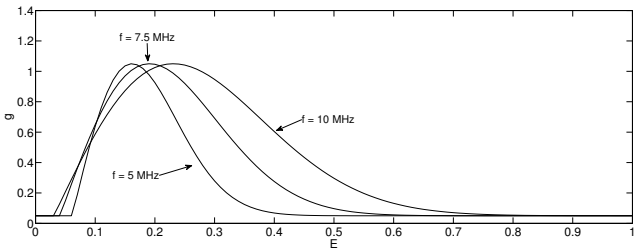

Figure 3.7. The speckle energy is empirically modeled by an US frequency dependent Rayleigh-like function of local entropy, $g(E;f)$.

CT input image and its local entropy map.

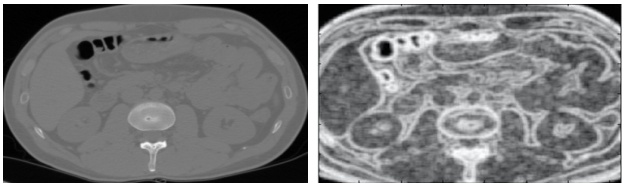

(a) (b)

Figure 3.8. The figure shows (a) a CT slice and (b) the map constructed based on its local entropy.

3.2.2. A Supervised Learning Approach

One of the simplest machine algorithms, k-NN, is a method for classification or regression, in which among the training data, k number of nearest neighbors are chosen for a test data and in return outputs are given. For example, a sample consisting many students with specifications height, weight, gender and their letter grades is known. When a student with his/her specifications (height, weight, gender) is given, the grade he/she will get is guessed from the sample by looking the distances of his/her features in the sample and giving the k number of grades, which are chosen from the grades with closest specifications in the sample. The final grade is set to whether the mean of k grades, minimum of the k grades or any statistical measurement wished. To sum up, in the training data, there is a large number of data with features and their corresponding label/output; and the output of a test data with the known features is guessed from the sample by looking the nearest neighbors. In k-NN, the nearest ones are measured with various methods, and among them, the mostly used one is calculated by Euclidean distances.

For the speckle creation based on this method, 7 US slices (B-mode), and an abdominal CT, acquired from a volunteer subject, are used. Then, the US slices are paired and registered to the corresponding CT images with the guidance of a radiologist. After this registration, a k-NN regressor is trained over these pairs, which will be describe below.

Since the envelope of the US signal follows Rician distribution [25], firstly, the US images are pre-processed to extract the envelope image approximately, by reversing the dynamic range mechanism applied in usual US systems. The dynamic range function, usually employed, in US machines is defined by

$$\tilde{s} = 255 \times \frac{20 \times log(s)}{DR} \tag{3.10}$$

where $\tilde{s}$, s and DR are representing the US pixel mapped to 0-255, the envelope value and the dynamic range parameter defined by the sonographer respectively.

The second step is to choose 'safe' regions of interest in that pairs, which are preferred with taking the faults (i.e, the deformation in US) into consideration. For each pixel in the regions of interest, N-bin normalized histograms of CT values of a 3D window, W_{CT} around the pixel are obtained as features of the training data. However, since rather than a structure, statistical info of tissue type is seeked in that window, the histogram of the subsample in the window of the same type (bone, air soft tissue) with the central pixel is obtained. For the property to be assigned to features, the pixel in the corresponding registered US slice (envelope, s) with a 2D window, W_{US}, are used. In this phase, there is a controller/test of uni-modality that when the pixels are passing the test, all the pixels are used; otherwise, the pixels with the same cluster of the central pixel are utilized. The test is done by forcing the sample with two-means clustering and if the means of two classes are enoughly far from each other, in which the threshold is set empricially, the second case above is faced, otherwise the first one. After that, Rician distribution is fit to each uni-modal set by means of the moment-matching method [26] and the fitted distribution's scale parameter, σ is associated with the features constructed with the corresponding W_{CT}.

The features and corresponding properties (mean scale parameters, σ's) are, hence, constitute the training data set. For any CT volume, from this point, the estimated σ values can be found by running the k-NN algorithm described above. In the estimation process, the mean scale parameter of the k nearest training samples is written as the estimated local speckle parameter of any pixel in that CT volume.

The motive for applying a machine learning algorithm to estimate σ parameters comes from the results shown in the Figure 3.9. As can be figured out, the Rice fit applied to the real US image gives good results as the simulation runs using these σ values. The only step is, then, to find the estimated parameters using the method described above.

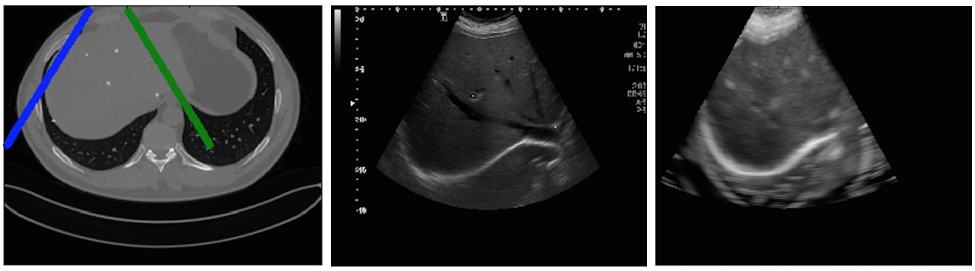

(a) (b) (c)

Figure 3.9. The figure shows a pair of CT (a) and US (b). The image (c) is the simulated output of the CT slice (b) with the scale parameters extracted from the US (b) data using the Rician fitting.

3.3. Single Ray Beam Formation

As reflected signal from each transducer element is acquired, it cannot be shown to the user with its bare form. Before that, some post-processes are required. These processes are for giving the simulation more realism benefiting the physics of the ultrasound.

First of them is the convolution of each ray with a Gaussian filter. This filter actually accounts for the form of ultrasonic wave in the radial direction. The filter is composed of a 1D Gaussian kernel with zero mean and standard deviation equal to the ultrasonic pulse length (usually twice the wavelength).

The next step is to make the signal images to visible to human eye by a logarithmic

scaling function (LS) as written below:

$$LS(x) = \frac{log(10^{\beta}x + 1)}{log(10^{\beta} + 1)} \tag{3.11}$$

where β is a parameter controllable by the user. A sample application of logarithmic scaling is illustrated in the Figure 3.10. As another post-process, depending on the

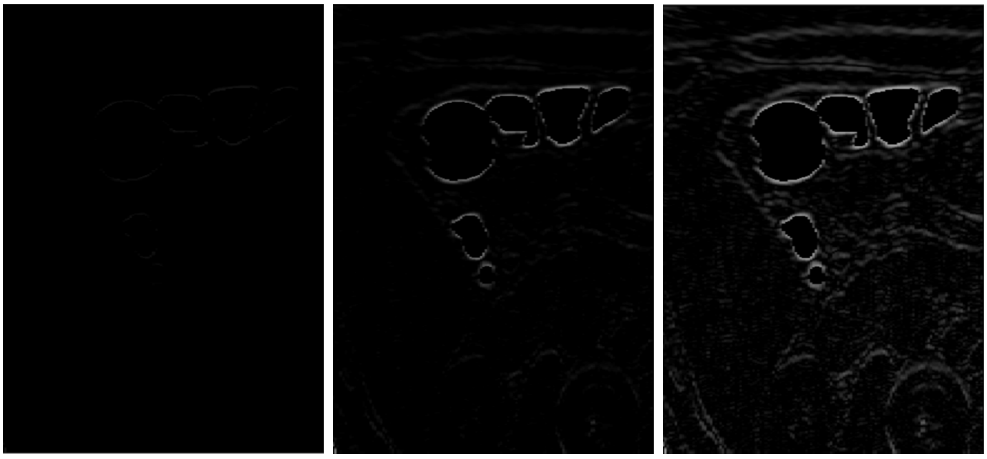

(a) Bare Reflection Signal (b) Ref. Signal with log scaling $\beta = 2$ (c) Ref. Signal with log scaling $\beta = 3$

Figure 3.10. The effect of logarithmic scaling.

choice, a gain compensation is applied to the images to reduce the effect of attenuation along the radial direction. The Figure 3.11 shows the effect of the attenuation compensation and supressing the strong reflections. In the last step, the scanlines are

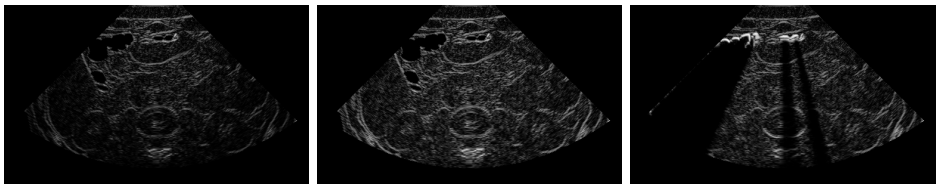

(a) Shadowing supressed (b) Shadowing supressed and Attenuation Gain used (c) Attenuation Gain used

Figure 3.11. The effects of attenuation gain and supression of shadowing.

converted to real spatial coordinates by interpolating, which is defined by the geometry

determined by the transducer specifications. In the Figure 3.12, the input CT image and corresponding scan-converted reflection-transmission images are shown.

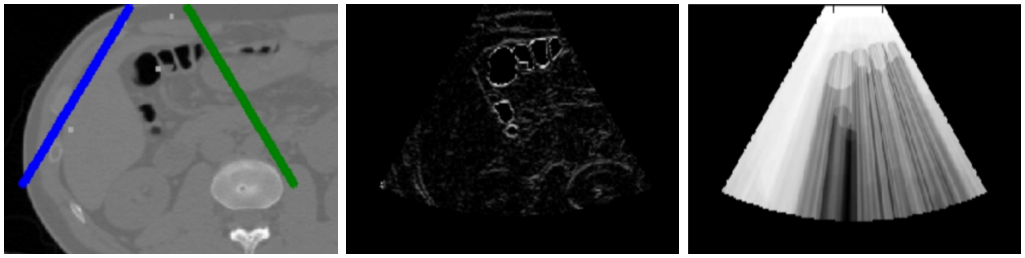

(a) CT image (b) Scan converted Ref Image (c) Scan converted Tra Image

Figure 3.12. Input CT image and corresponding reflection-transmission images with suppressed shadowing.

3.4. Multi Ray Beam Formation

The multi-ray US simulated image is constructed as a linear combination of shifted (delayed) $S(r)$'s. The combination coefficients are determined parametrically according to the user defined focusing level while the shifts are determined according to the assumed geometry. Figure 3.13 depicts the overall image formation geometry. The image formation for position $\mathbf{p}$ is given by,

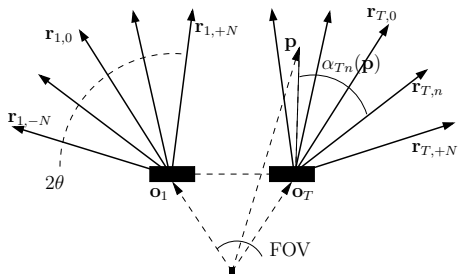

Figure 3.13. The multi-ray image formation geometry is composed of $2N+1$ rays per T transducers. Each transducer has a major view direction, $\mathbf{r}_{t0}$ and a field of view of 2θ, symmetric around $\mathbf{r}_{t0}$. Each pixel gets a contribution from all $T \times (2N+1)$ rays.

$$U(\mathbf{p}) = \sum_{t=1}^{T} \sum_{n=-N}^{N} w_{tn}(\mathbf{p}) S_{tn}(|\mathbf{p} - \mathbf{o}_t|) \tag{3.12}$$

$$w_{tn}(\mathbf{p}) = exp(-\frac{(\alpha_{tn}(\mathbf{p}))^2}{2\gamma^2}) \tag{3.13}$$

$$\alpha_{tn}(\mathbf{p}) = \angle((\mathbf{p} - \mathbf{o}_t), \mathbf{r}_{tn}) \tag{3.14}$$

where $\mathbf{p}$ is the pixel position, $\mathbf{o}_t$ is the tth transducer position, $\mathbf{r}_{tn}$ is the nth ray emanating from the tth transducer, γ is the free focusing parameter in degrees and S_{tn} is the associated 1D single-ray acoustic signal given by Equation 3.6.

With this method, the transmission and beam formation in the phased array transducer, which are introduced in the section related to beam formation in ultrasound imaging systems, are aimed to be mimiced. The weights, $w_{tn}(\mathbf{p})$, define the contribution of each ray, modeling transmit stage, in other words steering the beam while the shifts/delays ($|\mathbf{p} - \mathbf{o}_t|$) model the reception stage focusing.

As small notes, it can be said that; unlike the single ray beam formation, there is no need to convert the sampled pixels in this method since they (many points like $\mathbf{p}$) are chosen with the formation of a regular grid in cartesian coordinates. Other post-processing mechanisms follow the same scheme as applied in the single ray method. In the figure below, an example of the simulation output with the CT input next to it is shown.

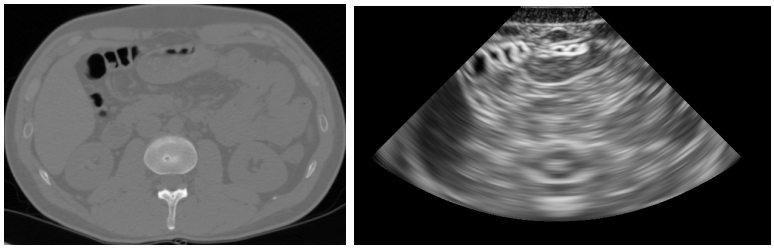

(a) CT input (b) The simulated output

Figure 3.14. The CT slice and the simulated image with 13 multirays and the parameters $f = 5MHz$, γ =2.54°.

4. RESULTS

The input CT slice shown in the Figure 4.1, was chosen from theCT volume of the size $512 \times 512 \times 243$, with in-plane resolution 0.68 mm $\times$ 0.68 mm and slice thickness 2 mm. The CT current and voltage were 246 mA and 120 kV. The data was stored in DICOM format. The probe position was set to be the center of the anterior side of an axial slice. The field of view, FOV was 90°. There were 128 ($T = 128$) transducers over a 6 cm range. The signal frequency, f, was set to 5. The Figure 4.1 shows the results simulated with these parameters.

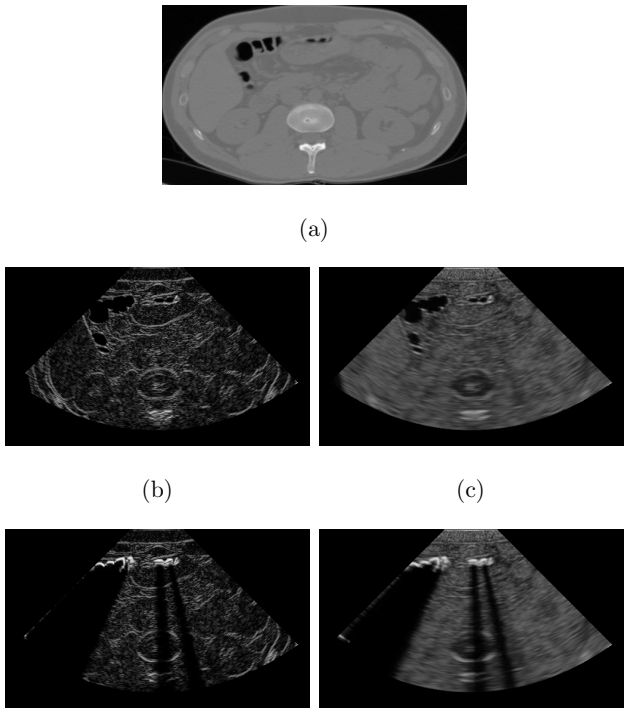

(a)

(b) (c)

(d) (e)

Figure 4.1. The figure shows (a) The input CT, (b) The simulated output with $\sigma = 0$ and shadowing supressed, (c) The simulated image with speckle based on local entropy and shadowing supressed, (d) The simulated output with $\sigma = 0$, (e) The simulated output with speckle based on local entropy.

With the same CT input, the results for various multirays and parameters were simuated (see Figure 4.2. The field of view was 90°, the transducer elements had the view (2θ) 60°.

For the speckle creation based on k-NN algorithm the following steps were taken. A CT volume was acquired with the parameters: 0.6 mm collimation, spiral pitch 0.6, 1.0mm slice thickness, 0.81 $mm \times 0.81$ mm in-plane spacing, voltage of 100 kVp, current of 432 mA. The subject was imaged in US examination immediately after the CT scan with Toshiba^{TM}Aplio 500 US system, using a curved probe at $5MHz$ and with 60° FOV. After the imaging, 7 CT-US pairs were registered with the guidance of a radiologist. Choosing the secure regions of interest, then, the 500-bin histograms of the CT regions with the window, W_{CT} of $15 \times 15 \times 15$ and the σ parameters Rician-fitted from the US regions with the window, W_{US} of $15 \times 15 \times 15$ were constructed. Out of 7 slices, one was chosen and the machine learning algorithm was run using the training data obtained from 6 pairs extracting the chosen's one to test the results. In the Figure 4.3, the simulated output with the CT and US pair is shown.

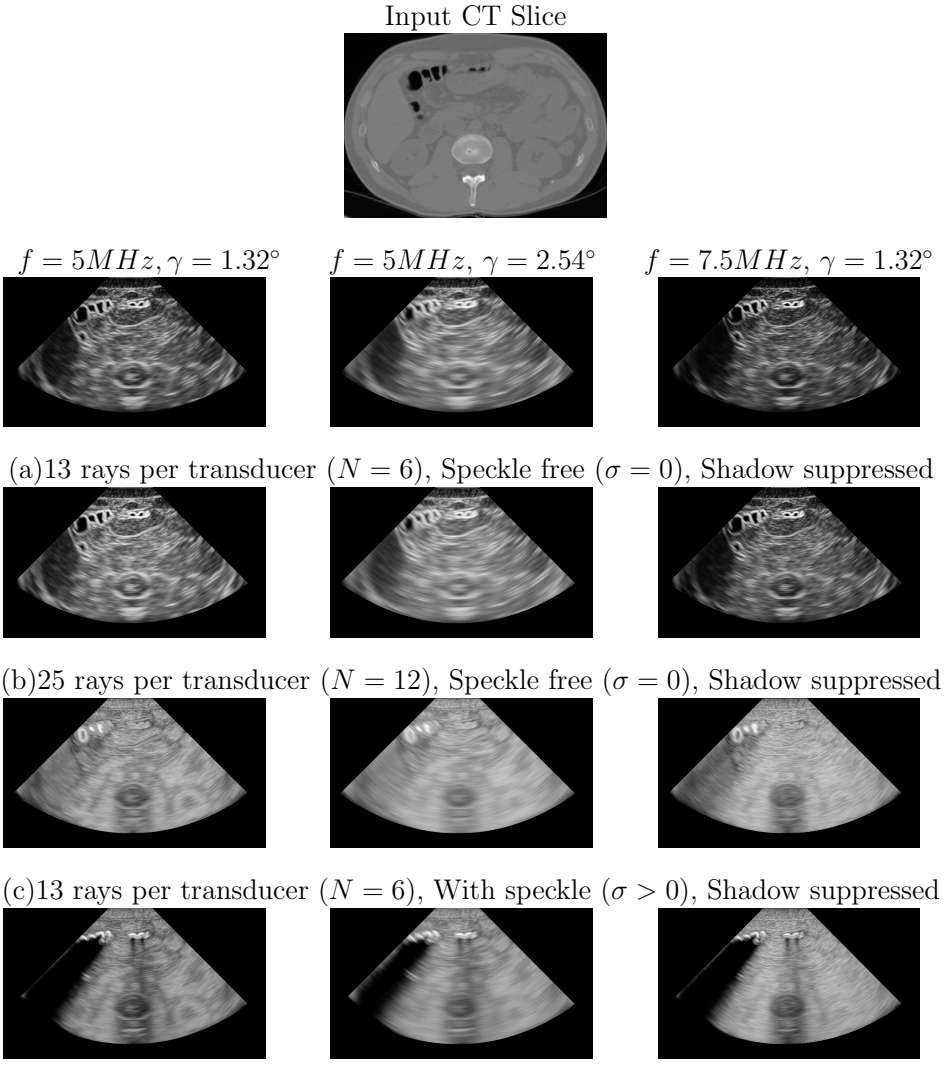

(a)13 rays per transducer ($N = 6$), Speckle free ($\sigma = 0$), Shadow suppressed

(b)25 rays per transducer ($N = 12$), Speckle free ($\sigma = 0$), Shadow suppressed

(c)13 rays per transducer ($N = 6$), With speckle ($\sigma > 0$), Shadow suppressed

(d)13 rays per transducer ($N = 6$), With speckle ($\sigma > 0$)

Figure 4.2. The effects of f, γ, N are depicted. (a),(b),(c) have shadow suppression while (d) does not. Increasing γ (decreased focusing) increased blurring for all cases. Increasing f changed the attenuation behaviour, esp. when the simulated speckle is added (d). Increasing N did not have much effect on simulated images.

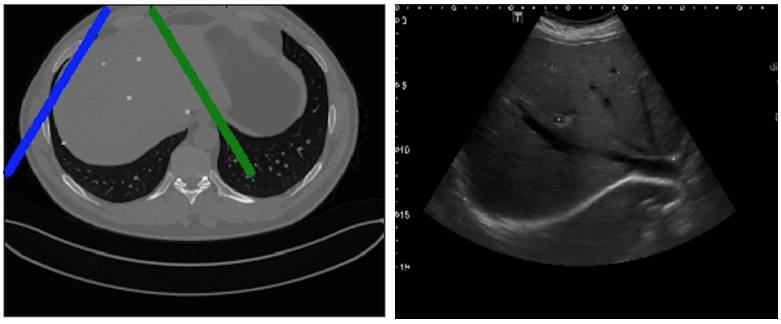

(a) (b)

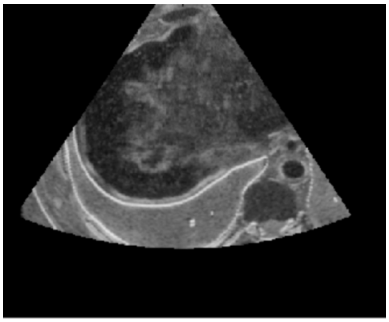

(c)

Figure 4.3. The figure shows (a) The CT slice of one of the pairs,also used for input for the simulation, (b) The US image of the pair, (c) The simulated image with the estimated scale parameters.

5. DISCUSSION AND CONCLUSION

The two sources of image contrast in US are reflection and scattering, the latter providing the main complementary information with respect to other modalities. The nonlinear dependencies of US images to scatterer density and size distributions, as well as modeling these distributions themselves, are challenging. Computationally costly solutions exist for the former, while the latter is an open problem. The challenge is even more demanding when a real-time simulation is needed.

The approach preseneted in this thesis pursues a previously proposed approach [14] due to its potential for real-time simulations. The novel multi-ray extension and speckle models introduce the focusing, frequency and local structure dependence, all based on US imaging physics. The preliminary simulation studies suggest that the proposed method is capable to reproducing these dependencies to a great extent. Namely, the effect of the focusing parameter in blurring and the effect of increasing frequency in attenuation effects can be observed. The speckle models, on the other hand, are the most controversial part of the system. The models are based on US image formation physics, with the assumption that the scale parameter σ reflecting, the scatterer distribution and the response of it, can be estimated. In the first method, the scale parameter is assumed to be correlated with the local entropy or in input CT images. In the second one, a machine learning algorithm, k-NN, is used to estimate the scale parameter.

Local entropy is a measure of inhomogeneity. With the assumption that the scatterers cause CT value fluctuations, high scatterer density and size jointly affects the inhomogeneity. High density/size at constant size/density increases inhomogeneity up to the level where we have so high density / large size that the CT cannot resolve, hence the inhomogeneity decreases. Further evaluations of this model are needed for an in-depth assessment. Following this reasoning, other measures of texture may also be considered for the scale parameter estimation.

The other method for speckle creation based on the k-NN algorithm tries to estimate the scale parameters using the pairs of registered CT and US slices. It assumes that given a feature set obtained by any CT volume, the scale parameter can be learned by extracting the scale parameters of the nearest neighbors of CT features. However, since the algorithm is the easiest machine algorithm, it may not estimate the parameters properly. The simulated output with these estimated parameters shows that it is the case. There is a structure coming from nowhere in the liver, though the histograms of the regions in the liver are almost the same. Another reason might be that the speckle modeling depends on the CT dose and resolution. Different regressors may be trained for different CT doses and resolutions.

A major drawback of the current algorithm is the lack of contrast at blood vessels. This is due to the low contrast of these regions in CT images. This is a fundamental problem due to the input data modality, namely CT. While multi-modal input is a viable approach, an easy workaround is preprocessing the CT data to segment the blood vessels. The segmentation masks can be used in simulation.

Since the cosine term in the reflection coefficient computation, reflecting the angle of the incident ray, is assumed to be 90° and only one echo is simulated (rather than multi-echoes), the method cannot reproduce ghosting and reverberation artifacts in its current form either. These artifacts are rather suppressed in modern US systems, leaving this as a minor simulation problem. However, it is possible to incorporate these effects on the single-ray 1D signal processing stage.

For a given pixel $\mathbf{p}$ and focusing parameter γ, the weights ($w_{tn}(\mathbf{p})$) and the shifts/delays ($|\mathbf{p} - \mathbf{o}_t|$) are constant. Hence, they can be pre-calculated and stored in a look-up-table, allowing real-time simulations.

REFERENCES

1. *Compatible Toshiba PVT-375BT Ultrasound Probe Transducer of Precise Life*, 2014, http://www.weamax.com/products-search/pz6a13112-cz5c963f3-compatible-toshiba-pvt-375bt-ultrasound-probe-transducer.html, [Accessed June 2015].

2. *Medical West Introduces New State-of-the-Art Imaging Technology*, 2015, http://www.medicalwesthospital.org/medical-west-introduces-new-state-of-the-art-imaging-technology-.php, [Accessed June 2015].

3. Szabo, T. L., *Diagnostic Ultrasound Imaging: Inside Out*, Elsevier Academic Press, Burlington, MA, USA, 2004.

4. Hindi, A., C. Peterson and R. Barr, "Artifacts in Diagnostic Ultrasound", *Reports in Medical Imaging*, Vol. 6, pp. 29–48, 2013.

5. Prince, J. and J. Links, *Medical Imaging Signals and Systems*, Pearson Education, Inc., New Jersey, USA, 2006.

6. *Mindray DC6 Ultrasound Machine*, 2015, http://www.cvsales.com/cvs/UltrasoundbyBrand/MindrayUltrasound/MindrayDC6.aspx, [Accessed June 2015].

7. *Doppler Ultrasound of An Artery*, 2015, http://www.webmd.com/heart-disease/doppler-ultrasound-of-an-artery,[Accessed June 2015].

8. Karadayi, K., C. Lee and Y. Kim, "Software-based Ultrasound Beamforming on Multi-core DSPs", *IEEE International Ultrasonics Symposium*, pp. 503–506, 2011.

9. *k-Wave Toolbox*, 2004, `http://www.k-wave.org/documentation/scanConversion.php`, [Accessed June 2015].

10. *Tutorial 1 - Basic Physics of Ultrasound and The Doppler Phenomenon*, 2009, `http://www.criticalecho.com/content/tutorial-1-basic-physics-ultrasound-and-doppler-phenomenon`, [Accessed June 2015].

11. Aiger, D. and D. Cohen-Or, "Real-time Ultrasound Imaging Simulation", *Real-Time Imaging*, Vol. 4, No. 4, pp. 263–274, 1998.

12. Ehricke, H.-H., "SONOSim3D: A Multimedia System for Sonography Simulation and Education with An Extensible Case Database", *European Journal of Ultrasound*, Vol. 7, No. 3, pp. 225–230, 1998.

13. Goksel, O. and S. E. Salcudean, "B-mode Ultrasound Image Simulation in Deformable 3-D Medium", *Medical Imaging, IEEE Transactions on*, Vol. 28, No. 11, pp. 1657–1669, 2009.

14. Wein, W., S. Brunke, A. Khamene, M. R. Callstrom and N. Navab, "Automatic CT-Ultrasound Registration for Diagnostic Imaging and Image-guided Intervention", *Medical image analysis*, Vol. 12, No. 5, pp. 577–585, 2008.

15. Shams, R., R. Hartley and N. Navab, "Real-time Simulation of Medical Ultrasound from CT Images", *Medical Image Computing and Computer-Assisted Intervention–MICCAI 2008*, pp. 734–741, 2008.

16. Hostettler, A., C. Forest, A. Forgione, L. Soler and J. Marescaux, "Real-time Ultrasonography Simulator Based on 3D CT-scan Images", *Studies in Health Technology and Informatics*, Vol. 111, pp. 191–193, 2005.

17. Wenjian, Q., W. Tiexiang, Z. Zhen, L. Zhicheng, L. Weisong, F. Xiang, J. Ying and G. Jia, "A Pilot Study on Simulation of Ultrasound from MRI Using

Ray-based Model", *Biomedical and Health Informatics (BHI), 2012 IEEE-EMBS International Conference on*, pp. 632–635, 2012.

18. *Image Showing CT Scan Slices*, 2008, `http://www.npac.syr.edu/projects/cpsedu/summer98summary/examples/hpf/hpf.html`, [Accessed June 2015].

19. Schneider, U., E. Pedroni and A. Lomax, "The Calibration of CT Hounsfield Units for Radiotherapy Treatment Planning", *Physics in Medicine and Biology*, Vol. 41, No. 1, p. 111, 1996.

20. Cobbold, R. S. C., *Foundations of Biomedical Ultrasound*, Oxford University Press, Inc., New York, NY, USA, 2007.

21. Jensen, J. A., "FIELD: A Program for Simulating Ultrasound Systems", *10TH Nordicbaltic Conference on Biomedical Imaging*, Vol. 4, pp. 351–353, 1996.

22. Kutter, O., R. Shams and N. Navab, "Visualization and GPU-accelerated Simulation of Medical Ultrasound from CT Images", *Computer Methods and Programs in Biomedicine*, Vol. 94, No. 3, pp. 250–266, 2009.

23. *k-Wave Toolbox*, 2004, `http://www.k-wave.org/documentation/hounsfield2density.php`, [Accessed June 2015].

24. Burckhardt, C. B., "Speckle in Ultrasound B-mode Scans", *Sonics and Ultrasonics, IEEE Transactions on*, Vol. 25, No. 1, pp. 1–6, 1978.

25. Insana, M. F., R. F. Wagner, B. S. Garra, D. G. Brown and T. H. Shawker, "Analysis of Ultrasound Image Texture via Generalized Rician Statistics", *Optical Engineering*, Vol. 25, No. 6, pp. 256743–256743, 1986.

26. *Rice/Rician Distribution*, 2008, `http://www.mathworks.com/matlabcentral/fileexchange/14237-rice- rician-distribution`, [Accessed June 2015].